SANDIA REPORT
SAND2010-0139
Unlimited Release
Printed January 2010

The Development of a High-Throughput Gradient Array Apparatus for the Study of Porous Polymer Networks

Bret J. Chisholm, James Bahr, Partha Majumdar, Elizabeth Lee, Kris Schiele, Michael Weisz and Shawn M. Dirk

Prepared by
Sandia National Laboratories
Albuquerque, New Mexico 87185 and Livermore, California 94550

Sandia is a multiprogram laboratory operated by Sandia Corporation,
a Lockheed Martin Company, for the United States Department of Energy's
National Nuclear Security Administration under Contract DE-AC04-94AL85000.

Approved for public release; further dissemination unlimited.

Sandia National Laboratories

Issued by Sandia National Laboratories, operated for the United States Department of Energy by Sandia Corporation.

NOTICE: This report was prepared as an account of work sponsored by an agency of the United States Government. Neither the United States Government, nor any agency thereof, nor any of their employees, nor any of their contractors, subcontractors, or their employees, make any warranty, express or implied, or assume any legal liability or responsibility for the accuracy, completeness, or usefulness of any information, apparatus, product, or process disclosed, or represent that its use would not infringe privately owned rights. Reference herein to any specific commercial product, process, or service by trade name, trademark, manufacturer, or otherwise, does not necessarily constitute or imply its endorsement, recommendation, or favoring by the United States Government, any agency thereof, or any of their contractors or subcontractors. The views and opinions expressed herein do not necessarily state or reflect those of the United States Government, any agency thereof, or any of their contractors.

Printed in the United States of America. This report has been reproduced directly from the best available copy.

Available to DOE and DOE contractors from
U.S. Department of Energy
Office of Scientific and Technical Information
P.O. Box 62
Oak Ridge, TN 37831

Telephone: (865) 576-8401
Facsimile: (865) 576-5728
E-Mail: reports@adonis.osti.gov
Online ordering: http://www.osti.gov/bridge

Available to the public from
U.S. Department of Commerce
National Technical Information Service
5285 Port Royal Rd.
Springfield, VA 22161

Telephone: (800) 553-6847
Facsimile: (703) 605-6900
E-Mail: orders@ntis.fedworld.gov
Online order: http://www.ntis.gov/help/ordermethods.asp?loc=7-4-0#online

SAND2010-0139
Unlimited Release
Printed January 2010

The Development of a High-Throughput Gradient Array Apparatus for the Study of Porous Polymer Networks

Bret J. Chisholm,[1,2] James Bahr,[1] Partha Majumdar,[1] Elizabeth Lee,[1] Kris Schiele,[1] and Michael Weisz[1] and Shawn M. Dirk,[3]

[1]Center for Nanoscale Science and Engineering,
North Dakota State University
Fargo, North Dakota 58102

[2]Department of Coatings and Polymeric Materials,
North Dakota State University
Fargo, North Dakota 58102

[3]Organic Materials Department,
Sandia National Laboratories, P.O. Box 5800
Albuquerque, New Mexico 87185-MS0888

Abstract

A gradient array apparatus was constructed for the study of porous polymers produced using the process of chemically-induced phase separation (CIPS). The apparatus consisted of a 60 element, two-dimensional array in which a temperature gradient was placed in the y-direction and composition was varied in the x-direction. The apparatus allowed for changes in opacity of blends to be monitored as a function of temperature and cure time by taking images of the array with time. The apparatus was validated by dispense a single blend composition into all 60 wells of the array and curing them for 24 hours and doing the experiment in triplicate. Variations in micron scale phase separation were readily observed as a function of both curing time and temperature and there was very good well-to-well consistency as well as trial-to-trial consistency. Poragen of samples varying with respect to cure temperature was removed and SEM images were obtained. The results obtained showed that cure temperature had a dramatic affect on sample morphology, and combining data obtained from visual observations made during the curing process with SEM data can enable a much better understanding of the CIPS process and provide predictive capability through the relatively facile generation of composition-process-morphology relationships. Data quality could be greatly enhanced by making further improvements in the apparatus. The primary improvements contemplated include the use of a

more uniform light source, an optical table, and a CCD camera with data analysis software. These improvements would enable quantification of the amount of scattered light generated from individual elements as a function of cure time.

In addition to the gradient array development, porous composites were produced by incorporating metal particles into a blend of poragen, epoxy resin, and crosslinker. The variables involved in the experiment were metal particle composition, primary metal particle size, metal concentration, and poragen composition. A total of 16 different porous composites were produced and characterized using SEM. In general, the results showed that pore morphology and the distribution of metal particles was dependent on multiple factors. For example, the use of silver nanoparticles did not significantly affect pore morphology for composites derived from decanol as the poragen, but exceptionally large pores were obtained with the use of decane as the poragen. With regard to the effect of metal particle size, silver nanoparticles were essentially exclusively dispered in the polymer matrix while silver microparticles were found in pores. For nickel particles, both nanoparticles and microparticles were largely dispersed in the polymer matrix and not in the pores.

CONTENTS

1.0 Introduction 11
2.0 Experimental 14
2.1 Materials 14
2.2 Instrumentation 16
3.0 Results and Discussion 17
3.1 Design and Fabrication of the Gradient Array Apparatus. 17
3.2 Validation of the Gradient Array Apparatus 21
4.0 Conclusions 37
5.0 References 37

FIGURES

Figure 1. Representative phase diagrams showing UCST behavior (left) and LCST behavior (right). 12
Figure 2. A schematic illustration describing morphology development associated with spinodal decomposition. 12
Figure 3. A schematic illustration of the high-throughput workflow that was initially developed for the study of porous polymer networks produced using CIPS. 14
Figure 4. Gradient array apparatus photos: (a) Side view of the gradient array plate apparatus with a fiber optic light source in the background; (b) Overhead view of the gradient array plate during operation. Digital displays on the right are gradient plate temperatures in degrees F (+/- 3 deg F) as measured from seven thermocouple probes uniformly spaced on a center line in the 5/8 inch thick aluminum base plate. Image B represents an image captured during an experiment. An image is taken once a minute by an overhead digital SLR camera for later import into a short movie file. The run time is displayed in minutes by the timer in the lower right corner. 18
Figure 5. A cross-sectional view of the gradient array plate depicting the assembly of the sub-components. 19
Figure 6. An image of the array of soft Buna o-rings potted on to a 4x8 inch glass plate with red silicone. Gluing the o-rings to glass creates sixty discrete 180µl wells that can be manually filled with resin blends using a repeat pipetter. After all of the wells are filled, a second glass plate is placed on top to seal in the polymer samples between two glass plates prior to heating on the thermal gradient plate apparatus. 20
Figure 7. An image of the o-ring and glass array substrate assembly illuminated by directing a very narrow light beam into the longest edge of the bottom glass plate. The lower glass plate appears red in the photo as white light internally reflects off of the red silicone potting compound

adhered to its upper surface while the upper glass plate is not illuminated. *Inset photo upper left*- Edge-on illumination produces a dramatic change in contrast between clear, one-phase samples compared to those that have undergone phase separation. The two phase systems become bright, translucent dots compared to the one phase blends since they scatter the captured light from below. 20
Figure 8. Images illustrating the reproducibility of the apparatus. The three images were all taken at 35 minutes from the start of the individual experiments. Each experiment produced a distinctive phase separation in the fourth row up from the bottom which corresponded to a cure temperature of approximately 80 °C. The darker panels on the right were imaged inside a dark tent to increase the image contrast whereas that array on the left was imaged without the tent. 21
Figure 9. Representative images of the array as a function of heating time utilizing a single polymer composition across the entire array. (a) before heating (time = 0); (b) 10 minutes after the start of heating; (c) 35 minutes after the start of heating; (d) 40 minutes after the start of heating; (e) 69 minutes after the start of heating; (f) 133 minutes after the start of heating; (e) 375 minutes after the start of heating; and (h) 1387 minutes after the start of heating. 23
Figure 10. Time required to reach the cloud point as a function of cure temperature. 24
Figure 11. SEM images of poragen-extracted materials crosslinked at different temperatures. The samples were obtained from the 5th column from the left in the array shown in Figure 9. 25
Figure 12. A schematic illustration of the experimental design used to investigate the effect of metal particles on sample morphology. 26
Figure 13. SEM micrographs of the metal particles used for the experiment. (A) silver nanoparticles; (B) nickel nanoparticles; (C) silver microparticles; and (D) nickel microparticles. 27
Figure 14. SEM micrographs of 50/50 wt./wt. composites of metal particles in the epoxy network. (A) silver nanoparticles; (B) nickel nanoparticles; (C) silver microparticles; and (D) nickel microparticles. 28
Figure 15. SEM micrographs of porous polymer networks derived from Ep/MCHA/decane (left) and Ep/MCHA/decanol (right). 29
Figure 16. SEM micrographs of porous composites based on silver nanoparticles: (A) 25 wt. % Ag nanoparticles and decane as the poragen; (B) 25 wt. % Ag nanoparticles and decanol as the poragen; (C) 50 wt. % Ag nanoparticles and decane as the poragen; (D) 50 wt. % Ag nanoparticles and decanol as the poragen. 30
Figure 17. SEM micrographs of porous composites based on silver nanoparticles: (A) 25 wt. % Ag nanoparticles and decane as the poragen; (B) 25 wt. % Ag nanoparticles and decanol as the poragen; (C) 50 wt. % Ag nanoparticles and decane as the poragen; (D) 50 wt. % Ag nanoparticles and decanol as the poragen. 31
Figure 18. SEM micrographs of porous composites based on silver microparticles: (A) 25 wt. % Ag microparticles and decane as the poragen; (B) 25 wt. % Ag microparticles and decanol as the poragen; (C) 50 wt. % Ag microparticles and decane as the poragen; (D) 50 wt. % Ag microparticles and decanol as the poragen. 32

Figure 19. SEM micrographs of porous composites based on silver microparticles: (A) 25 wt. % Ag microparticles and decane as the poragen; (B) 25 wt. % Ag microparticles and decanol as the poragen; (C) 50 wt. % Ag microparticles and decane as the poragen; (D) 50 wt. % Ag microparticles and decanol as the poragen. 33
Figure 20. SEM micrographs of porous composites based on nickel nanoparticles: (A) 25 wt. % Ni nanoparticles and decane as the poragen; (B) 25 wt. % Ni nanoparticles and decanol as the poragen; (C) 50 wt. % Ni nanoparticles and decane as the poragen; (D) 50 wt. % Ni nanoparticles and decanol as the poragen. 34
Figure 21. SEM micrographs of porous composites based on nickel nanoparticles: (A) 25 wt. % Ni nanoparticles and decane as the poragen; (B) 25 wt. % Ni nanoparticles and decanol as the poragen; (C) 50 wt. % Ni nanoparticles and decane as the poragen; (D) 50 wt. % Ni nanoparticles and decanol as the poragen. 35
Figure 22. SEM micrographs of porous composites based on nickel microparticles: (A) 25 wt. % Ni microparticles and decane as the poragen; (B) 25 wt. % Ni microparticles and decanol as the poragen; (C) 50 wt. % Ni microparticles and decane as the poragen; (D) 50 wt. % Ni microparticles and decanol as the poragen. 36
Figure 23. SEM micrographs of porous composites based on nickel microparticles: (A) 25 wt. % Ni microparticles and decane as the poragen; (B) 25 wt. % Ni microparticles and decanol as the poragen; (C) 50 wt. % Ni microparticles and decane as the poragen; (D) 50 wt. % Ni microparticles and decanol as the poragen. 37

NOMENCLATURE

DOE	Department of Energy
NDSU	North Dakota State University
CIPS	Chemically induced phase separation
UCST	upper critical solution temperature
LCST	lower critical solution temperature
Ep	bisphenol-A-diglycidylether
MCHA	4,4'-methyl bis(cyclohexylamine)
De	decane
Dol	*n*-decanol
Ag NP	silver nanoparticles
Ag MP	silver microparticles
Ni NP	Nickel nanoparticles
Ni MP	Nickel microparticles
SEM	scanning electron microscope
SNL	Sandia National Laboratories

1.0 Introduction

Porous polymer materials are of interest for a wide variety of applications such as tissue scaffolds,[1] controlled release,[2] chromatography,[3] low-k dielectrics,[4] separation membranes,[5] piezoelectric materials,[6] chemical sensors,[7,8] hydrogen storage materials,[9,10] and battery electrodes.[11] Several general methods for creating porous polymers have been described. These methods include conventional foaming techniques involving a non-reactive gas,[12] emulsion-templating,[13,14] thermally-induced phase separation,[15] chemically-induced phase separation,[16] selective degradation of block copolymers,[17] and molecular imprinting.[18] Relative to the other methods for producing porous polymer materials, chemically-induced phase separation (CIPS) probably provides the greatest versatility with respect to the range of materials that can be generated. In addition, the process to produce porous materials using CIPS is relatively straightforward and a large number of readily available starting materials can be utilized.

The process for producing porous polymer materials using CIPS involves crosslinking of a homogeneous blend comprised of reactive precursors and a non-reactive component referred to as a poragen.[16,19] Due to the increase in the free energy of mixing that occurs as reaction takes place between the reactive precursors, the poragen phase separates from the mixture during the process of crosslinking. Porosity is generated by removal of the poragen from the crosslinked material using an extraction or evaporation process. The pore size, pore shape, and pore size distribution obtained with this process is a result of the complex interaction between the thermodynamics of mixing, kinetics of crosslinking, and kinetics of phase separation.

The well-known Flory-Huggins[20] equation (I) that describes the free energy of mixing (ΔG_{mix}) for a blend of a polymer and solvent can be used as a basis to understand the thermodynamics of CIPS.

$$\Delta G_{mix}=RT(n_{pol}\ln ø_{pol}+ n_{sol}\ln ø_{sol}+\chi ø_{pol} n_{sol}) \qquad \text{(I)}$$

For this equation, R is the gas constant, T is temperature, n_{pol} is the number of polymer molecules in moles, n_{sol} is the number of solvent molecules in moles, $ø_{pol}$ is the volume fraction of polymer, $ø_{sol}$ is the volume fraction of solvent, and χ is the interaction parameter which accounts for intermolecular interactions between polymer and solvent molecules. χ is not a constant; it depends on temperature, composition, and pressure. Huggins[21] experimentally showed that χ varies linearly with the inverse of temperature:

$$\chi = a + b/T \qquad \text{(II)}$$

Based on χ, two basic types of phase behavior are observed. If χ is positive and increases linearly with temperature, an upper critical solution temperature (UCST) is observed. In contrast, if χ is negative and decreases linearly with temperature, a lower critical solution temperature (UCST) is observed. Figure 1 displays a representative phase diagram showing UCST behavior as well as a phase diagram showing LCST behavior. The phase diagrams

exhibit three phases, namely, a stable phase, metastable phase, and a region in which spinodal decomposition occurs. If the temperature of a stable polymer solution is changed such that the region of spinodal decomposition is entered, phase separation occurs by a mechanism which proceeds in stages, as illustrated schematically in Figure 2. Initially, a co-continuous morphology is developed which proceeds to the formation of a dispersed phase morphology. In contrast, entering the metastable region results in phase separation by a nucleation and growth mechanism in which a dispersed phase morphology consisting of spherical domains is produced.

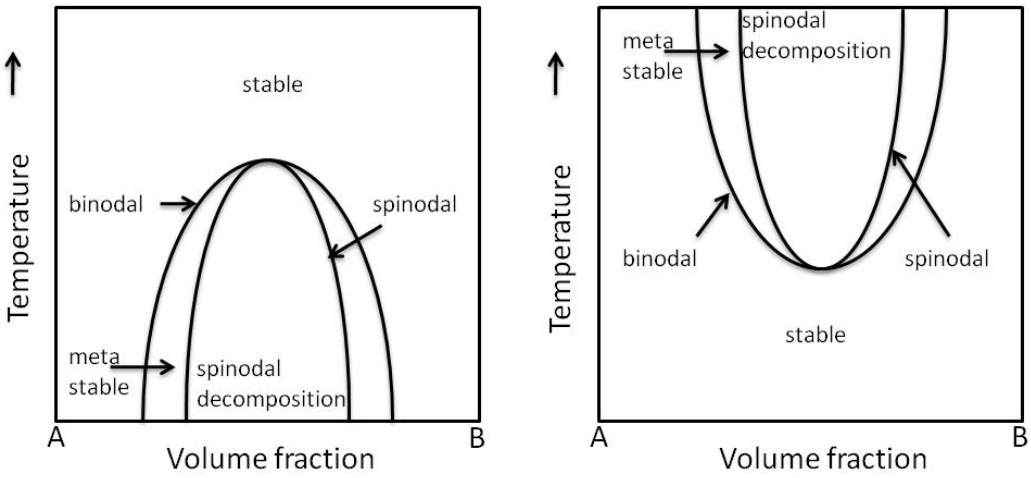

Figure 1. Representative phase diagrams showing UCST behavior (left) and LCST behavior (right).

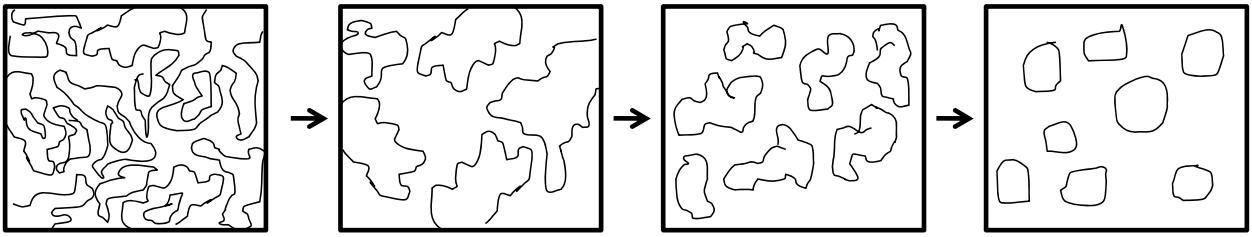

Figure 2. A schematic illustration describing morphology development associated with spinodal decomposition.

For CIPS, a stable solution is transformed into a phase separated material without a change in temperature. Phase separation in CIPS is the result of the decrease in entropy created by the increase in polymer molecular weight that occurs as a result of crosslinking reactions. Kiefer and coworkers[16] modified the Flory-Huggins equation so that it was applicable to reactive solutions. The modification took into account the change in the number of polymer molecules with functional group conversion and allowed for the construction of phase diagrams based on conversion at a constant temperature.

While thermodynamic models based on first principles are useful for identifying systems that will undergo CIPS, they do not allow for an accurate prediction of morphology because the

morphology produced with CIPS depends strongly on molecular mobility which changes dramatically as crosslinking proceeds. For example, pore size for materials that undergo phase separation by a nucleation and growth mechanism will be a result of the competition that exists between the reduction in free energy achieved by the nucleation and growth of pores and the ability of solvent molecules to diffuse through the polymer network that is increasing in viscosity as crosslinking proceeds. Due to the complexity of pore formation associated with CIPS, extensive structure-process-property relationships are needed to understand the influence of these variables on material properties.

The application of high-throughput/combinatorial methods for the generation structure-process-property relationships for polymer materials has been shown to be very powerful.[22-24] The ability to generate and characterize relatively large numbers of materials within a relatively short period of time enables the multivariable experiments required to identify complex interactions between variables. As a result of a previous project sponsored by Sandia, the authors constructed a high-throughput/combinatorial workflow for the generation of extensive structure-process-property relationships for porous polymer materials produced with the process of CIPS. Figure 3 provides a schematic of the workflow that was developed. With this workflow, individual samples were prepared using automation and curing was done simultaneously at a specific temperature in a conventional oven. As a result of this project, it was found that considerable information could be gained by simply monitoring changes in opacity of the blends as they cured. By monitoring opacity, blends that undergo CIPS could be easily identified. As a result, a gradient array format for curing blends was contemplated that would enable relationships between time, temperature, and blend composition to be readily determined for the process of CIPS. This document describes the design, fabrication, and validation of the high-throughput gradient array apparatus. In addition to this work, at the request of Shawn Dirk, a series of porous polymer materials were prepared and characterized that possessed conductive particles. The results of this additional work are also described in this document.

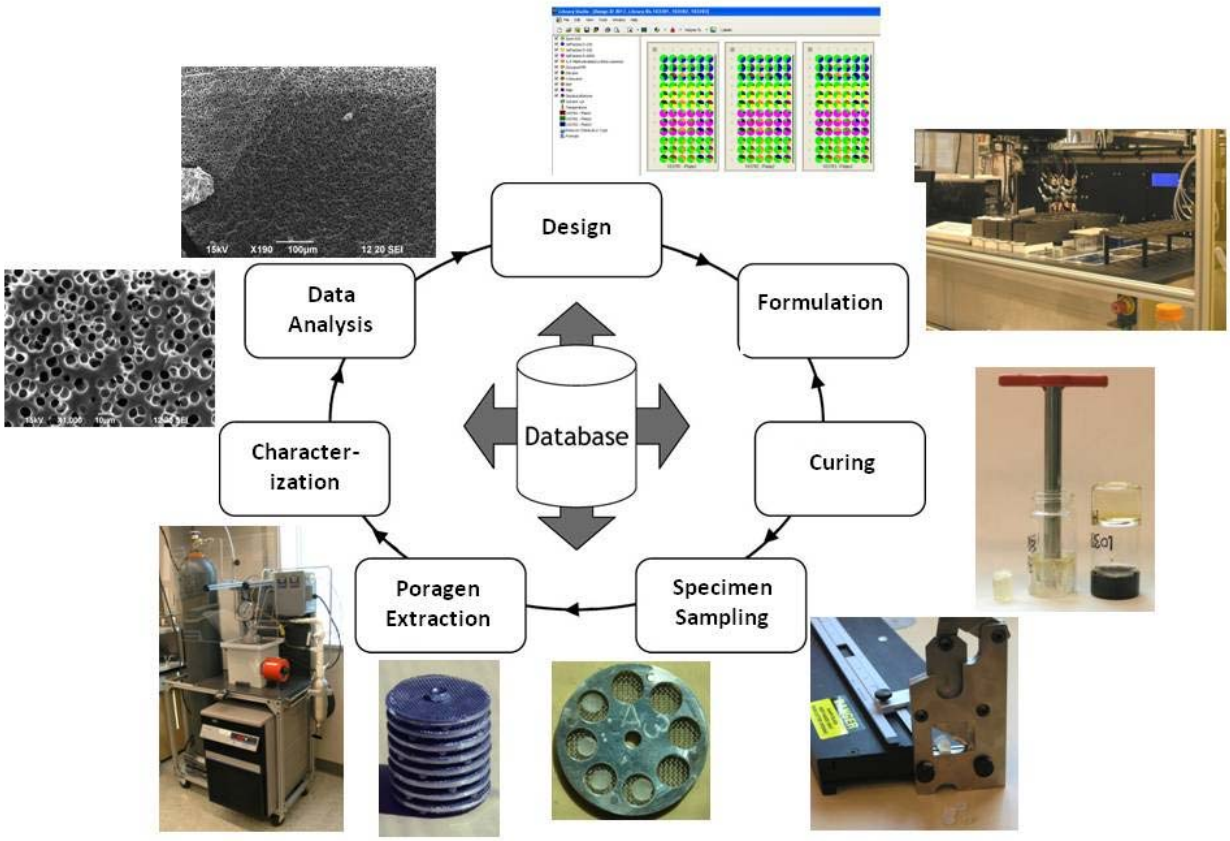

Figure 3. A schematic illustration of the high-throughput workflow that was initially developed for the study of porous polymer networks produced using CIPS.

2.0 Experimental

2.1 Materials

Table I describes the materials used for the experiment, and Table II describes each of the blends prepared.

Table I. A description of the starting materials used for the study.

Material ID	Description	Trade Name	Manufacturer
Ep	Bisphenol –A- diglycidylether	Epon™ Resin 825	Hexion
MCHA	4,4'-methylenebis(cyclohexylamine)	----	Aldrich
De	Decane	----	Aldrich
Dol	n-Decanol	----	Aldrich

Ag NP	Silver nanoparticle	----	Aldrich
Ag MP	Silver microparticle	----	Inframat Advanced Materials
Ni NP	Nickel nanoparticle	----	Aldrich
Ni MP	Nickel microparticle	----	Aldrich

Table II. Composition of the each of the blends prepared. MCHA was used as a crosslinker. All weights are in grams.

Sample ID	Wt. Ep	Wt. Crosslinker	Poragen	Wt. Poragen	Particle	Wt. Particle
MCHA	3.50	1.02	----	----	----	----
MCHA-60Dol	3.50	1.02	Dol	5.09	----	----
MCHA-40De	3.50	1.02	De	1.99	----	----
MCHA-40Dol	3.50	1.02	Dol	2.26	----	----
MCHA-50Ag NP	3.50	1.02	----	----	Ag NP	2.26
MCHA-50Ag MP	3.50	1.02	----	----	Ag MP	2.26
MCHA-50Ni NP	3.50	1.02	----	----	Ni NP	2.26
MCHA-50Ni MP	3.50	1.02	----	----	Ni MP	2.26
MCHA-40De-25Ag NP	3.50	1.02	De	1.99	Ag NP	1.13
MCHA-40De-50Ag NP	3.50	1.02	De	1.99	Ag NP	2.26
MCHA-40De-25Ag MP	3.50	1.02	De	1.99	Ag MP	1.13
MCHA-40De-50Ag MP	3.50	1.02	De	1.99	Ag MP	2.26

MCHA-40De-25Ni NP	3.50	1.02	De	1.99	Ni NP	1.13
MCHA-40De-50Ni NP	3.50	1.02	De	1.99	Ni NP	2.26
MCHA-40De-25Ni MP	3.50	1.02	De	1.99	Ni MP	1.13
MCHA-40De-50Ni MP	3.50	1.02	De	1.99	Ni MP	2.26
MCHA-40Dol-25Ag NP	3.50	1.02	Dol	2.26	Ag NP	1.13
MCHA-40Dol-50Ag NP	3.50	1.02	Dol	2.26	Ag NP	2.26
MCHA-40Dol-25Ag MP	3.50	1.02	Dol	2.26	Ag MP	1.13
MCHA-40Dol-50Ag MP	3.50	1.02	Dol	2.26	Ag MP	2.26
MCHA-40Dol-25Ni NP	3.50	1.02	Dol	2.26	Ni NP	1.13
MCHA-40Dol-50Ni NP	3.50	1.02	Dol	2.26	Ni NP	2.26
MCHA-40Dol-25Ni MP	3.50	1.02	Dol	2.26	Ni MP	1.13
MCHA-40Dol-50Ni MP	3.50	1.02	Dol	2.26	Ni MP	2.26

2.2 Instrumentation

SEM images were taken with the JEOL JSM-6300 scanning electron microscope available at NDSU or with a FEG-SEM JEOL 6700 that was available within the Characterization Facility at the University of Minnesota.

3.0 Results and Discussion

3.1 Design and Fabrication of the Gradient Array Apparatus.

If there exists a difference in refractive index between the poragen and the crosslinked epoxy network, significant information regarding the process of CIPS can be obtained by monitoring opacity of samples as a function time and temperature. To efficiently extract this information, the thermal gradient array apparatus displayed in Figure 4 was conceptualized, built, and tested. The thermal plate itself is constructed out of a thick 12x5 inch aluminum lower plate and a top plate made of ¼ inch thick aluminum. The top plate serves as both the guard heater, minimizing heat loss to the surroundings, and the primary clamp to prevent the assembly from leaking. The wide lower plate provides a ¾" buffer zone between the plate edges and the outermost polymer samples to minimize undesirable edge effects. The bottom and sides of the thick thermal plate are surrounded by 2 inches of semi-rigid ceramic fiber insulation board as well as ceramic fiber blankets to support the weight of the block and minimize heat loss. The top, however, remains un-insulated to allow camera images to be taken of the samples from above.

The un-insulated top is protected from heat loss by providing a guard heater in the form of the top clamping plate. This top plate is independently temperature controlled from the primary gradient plate below it. This allows it to receive the extra heating power needed to both maintain the top gradient plate at the set temperature and to supply the power lost to heating of the air above it. Since the guard heater is heated to the same thermal gradient as the primary gradient array, the heat loss from the samples is minimized due to the low temperature differential between the lower and upper gradient plates anywhere along their length.

Digital temperature controllers are used to maintain the desired temperature set point at each end of the thermal gradient. Five additional digital temperature readouts were added to give an indication of the temperature stability and uniformity. A chilled liquid is circulated through one end of the gradient plate to remove excess heat from the cooler end of the gradient.

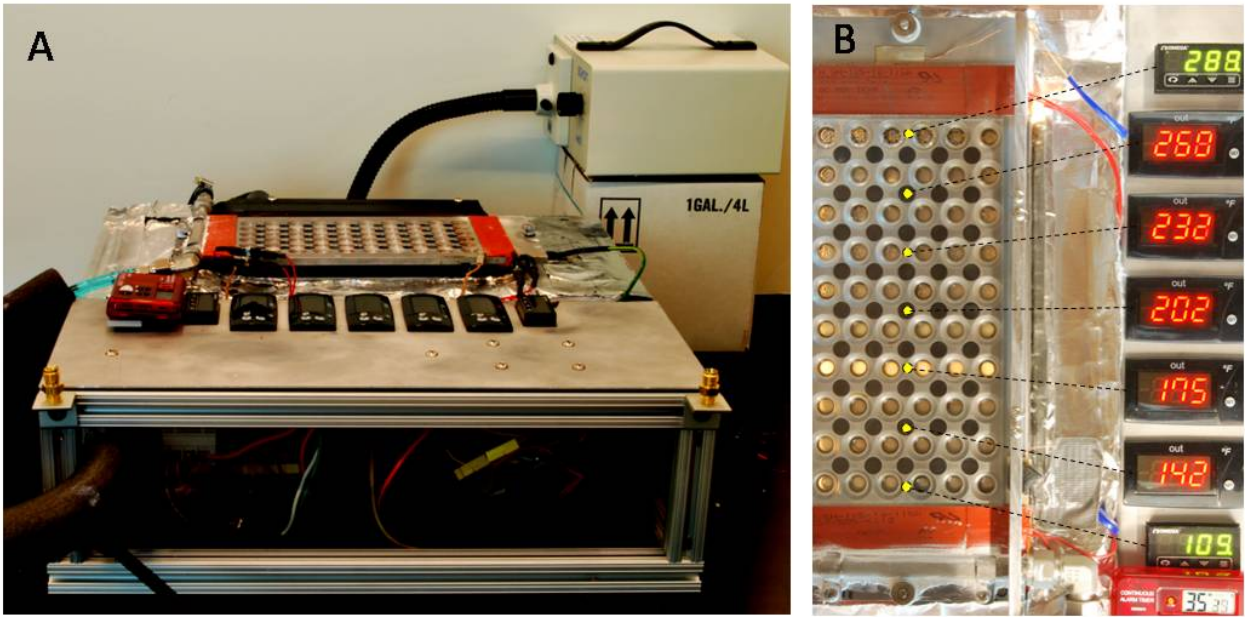

Figure 4. Gradient array apparatus photos: (a) Side view of the gradient array plate apparatus with a fiber optic light source in the background; (b) Overhead view of the gradient array plate during operation. Digital displays on the right are gradient plate temperatures in degrees F (+/- 3 deg F) as measured from seven thermocouple probes uniformly spaced on a center line in the 5/8 inch thick aluminum base plate. Image B represents an image captured during an experiment. An image is taken once a minute by an overhead digital SLR camera for later import into a short movie file. The run time is displayed in minutes by the timer in the lower right corner.

The polymer sample array plate is separate from the thermal gradient plate and is constructed of o-rings sandwiched between two glass plates. This approach allows the polymer array plate to be easily removed from the thermal gradient imaging station after an experiment. The cross-sectional breakdown of the polymer sample array and how it fits together with the top clamp plate and bottom gradient plate is shown in Figure 5. Placing the polymer samples directly on the aluminum plate would have given the best heat transfer, but glass was chosen as an intermediate substrate to facilitate through-sample lighting and provide ease of sample removal.

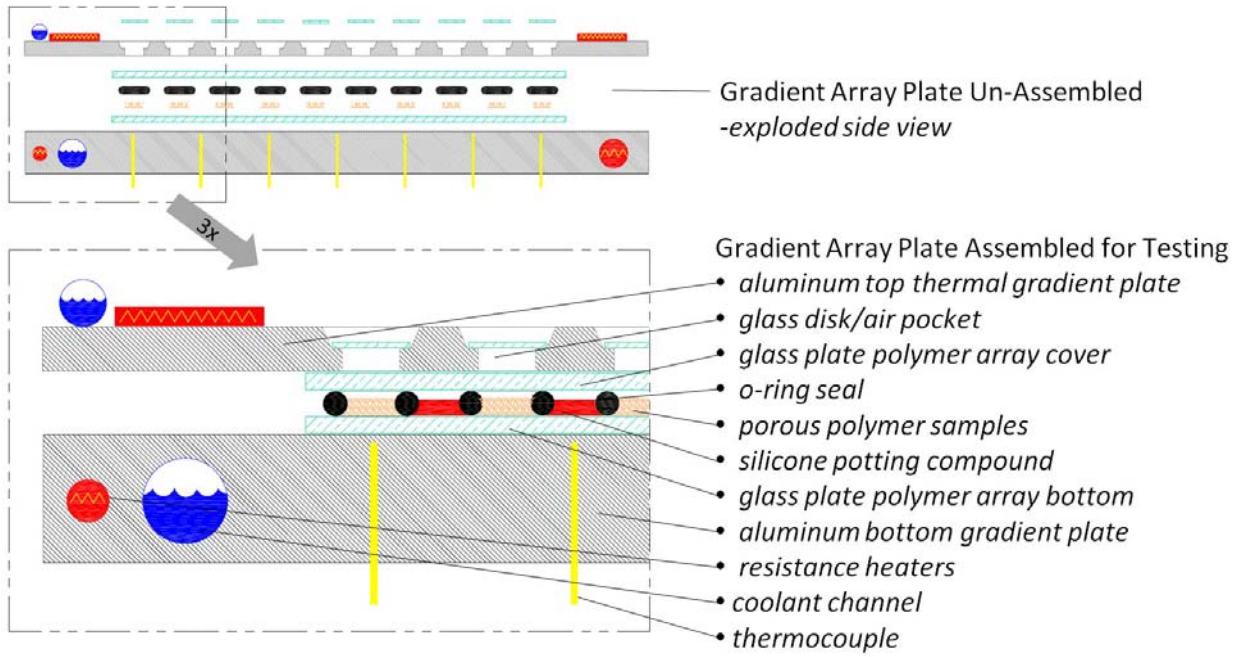

Figure 5. A cross-sectional view of the gradient array plate depicting the assembly of the sub-components.

The gradient plate is heated by two cartridge heaters embedded across its width at both ends. A water coolant journal was machined into the cold end of the gradient plate and fitted with a static mixing element to improve the heat transfer between the coolant and the aluminum journal walls. After exiting the coolant journal, the cold liquid is then directed up to a contact heat exchanger attached to the top clamp plate to remove excess heat before returning to the chiller.

The top clamp plate has holes machined over every polymer sample so that they can be seen from above. In addition, these holes have a shoulder machined into them to receive a small glass disk creating an air pocket above each sample. This simple addition provides insulation and reduces heat loss from the polymer samples in a region where they are not in direct contact with the lower or upper gradient plates while maintaining the visibility of the sample.

Polymer gradient plates are prepared by placing sixty Buna o-rings on a 4x8 inch glass plate using a template to ensure uniform spacing. The o-ring plate is then mounted in the apparatus so that high temperature red liquid silicone potting compound can be applied to the empty spaces between the o-rings. Once cured, the potting compound serves to hold the o-rings in place while they are filled with polymer test resins prior to testing. Without the potting compound in place, the o-rings would float up as the polymer samples are dispensed into them resulting in severe leakage and cross contamination. A prepared array plate ready for deposition is shown in Figure 6.

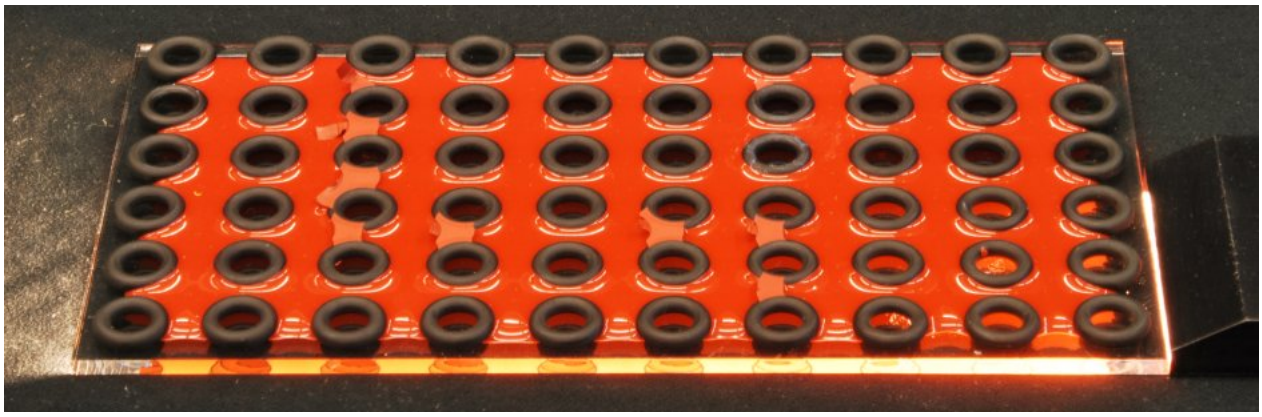

Figure 6. An image of the array of soft Buna o-rings potted on to a 4x8 inch glass plate with red silicone. Gluing the o-rings to glass creates sixty discrete 180µl wells that can be manually filled with resin blends using a repeat pipetter. After all of the wells are filled, a second glass plate is placed on top to seal in the polymer samples between two glass plates prior to heating on the thermal gradient plate apparatus.

Immediately after all 60 blends have been dispensed into the potted o-rings, a second glass plate of equal size is placed on top to seal off the samples. This blend array "sandwich" is then loaded onto the gradient array plate apparatus and clamped in place. Illumination of the array is provided by an adjustable intensity fiber optic light source fitted with a narrow "slit" aperture. The slit is actually the optical fiber bundle mashed out into a long thin strip. This unique lighting fixture produces an intense, even light source that is ideal for edge-on or oblique lighting situations. A close up photograph of the sample lighting configuration can be seen in Figure 7.

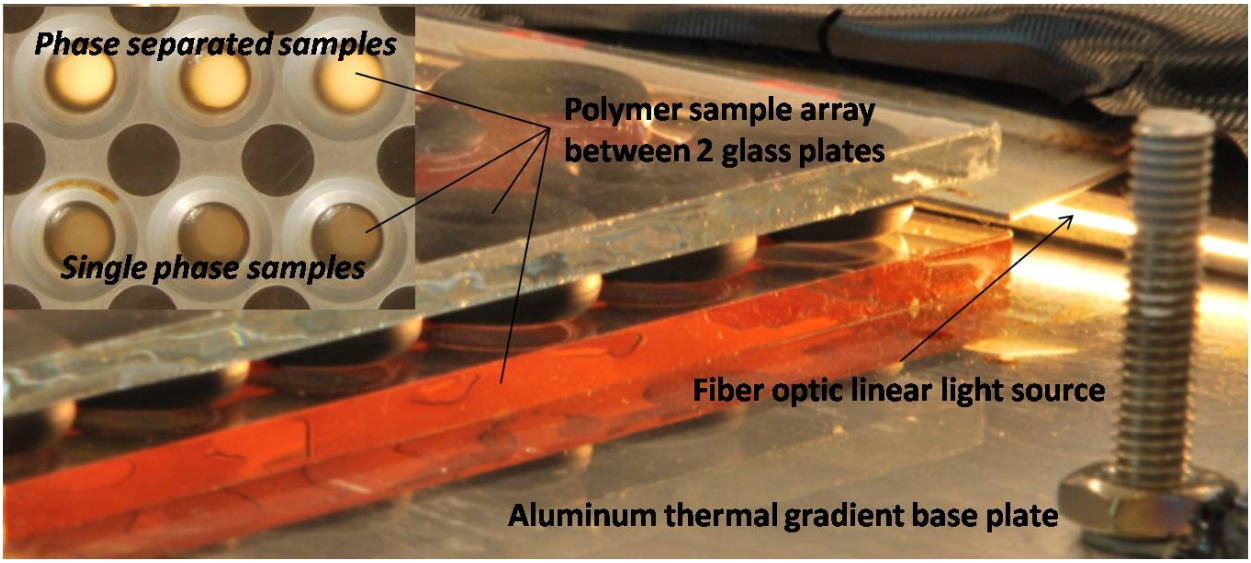

Figure 7. An image of the o-ring and glass array substrate assembly illuminated by directing a very narrow light beam into the longest edge of the bottom glass plate. The lower glass plate appears red in the photo as white light internally reflects off of the red silicone potting compound adhered to its upper surface while the upper glass plate is not

illuminated. *Inset photo upper left*- Edge-on illumination produces a dramatic change in contrast between clear, one-phase samples compared to those that have undergone phase separation. The two phase systems become bright, translucent dots compared to the one phase blends since they scatter the captured light from below.

Illuminating the polymer samples from below allows the entire apparatus to be placed inside a dark tent for the duration of the experiment. It is then possible to use long exposures of 45 seconds to capture the dim light that is transmitted through the polymer samples. Extraneous light is blocked by the opaque aluminum top plate, further enhancing the sample to sample contrast.

3.2 Validation of the Gradient Array Apparatus

Validation experiments were done using the blend, MCHA-60Dol, which had been previously shown to undergo CIPS. This blend was deposited in every position within the array in order to determine consistency of phase behavior and porosity between columns of the array. Deposition was done at room temperature and once complete, the temperature gradient was generated by running the array plate in the thermal gradient apparatus. Images were collected every minute for 24 hours from the point of heating. The same experiment was then replicated two more times. Figure 8 shows images obtained at 35 minutes for each of the three experiments.

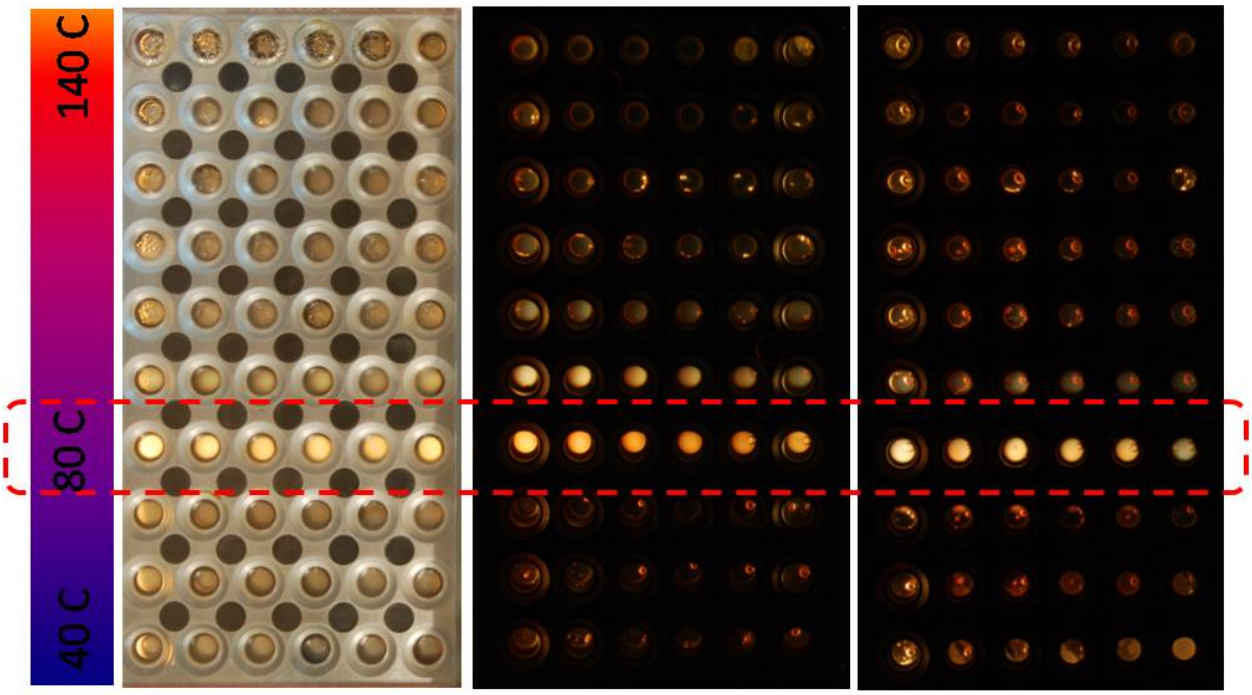

Figure 8. Images illustrating the reproducibility of the apparatus. The three images were all taken at 35 minutes from the start of the individual experiments. Each experiment produced a distinctive phase separation in the fourth row up from the bottom which corresponded to a cure temperature of approximately 80 °C. The darker panels on the

right were imaged inside a dark tent to increase the image contrast whereas that array on the left was imaged without the tent.

The results from all three experiments indicated that the thermal gradient plate was very isotherm across the rows. No edge effects were observed, and the experiments were consistent from one run to the next. The results of this testing suggest that the device could be used with a different polymer composition in each of the six columns to generate a two dimensional, 60-element compositional and thermal array. Sequential imaging provides the third dimension of time to the data collected from a single experiment. Validation experiments were run over a 24 hour period. For the particular blend used for the validation experiments, most of the changes in opacity occurred within the first few hours.

Eight images from a complete run are pictured in Figure 9. The photos in Figure 9 where taken in a dark tent used to block out all of the outside light allowing only the light transmitted through the polymer samples to be photographed. The sample arrays were lit from the left side by the fiber optic light source which resulted in the samples closer to the light source appearing slightly brighter than those on the right side. Elapsed time from the start of the heating process is shown in the lower right corner of each photograph. For the image at time zero (Figure 9a), all of the wells were relatively bright which was due to the fact that the blends at room temperature were stable, two-phase dispersions. 10 minutes after the start of the heating process (Figure 9b), all of the samples were dim because they had become miscible, one-phase materials. This result indicates that, without the formation of crosslinks, MCHA-60Dol exhibits UCST behavior with the UCST being between ambient temperature and 140 °F (i.e. 60 °C). Any phase separation occurring beyond this point in the experiment was due to increases in polymer molecular resulting from crosslinking reactions. After 35 minutes of heating (Figure 9c), the wells in the 4th row from the bottom of the array had undergone phase separation as indicated by the relative brightness of the samples in this row. According to the temperature readout, this row corresponded to a cure temperature of approximately 190 °F (i.e. 88 °C). After 40 minutes of heating (Figure 9d), the 3rd row from the bottom also had undergone phase separation as indicated by the change in brightness. The cure temperature associated with this row was approximately 176 °F (i.e. 80 °C). After 69 minutes of heating (Figure 9e), the 2nd row from the bottom corresponding to a temperature of 158 °F (i.e. 70 °C) had undergone phase separation. After 133 minutes of heating (Figure 9f), the bottom row corresponding to a temperature of 140 °F (i.e. 60 °C) underwent phase separation. After 375 minutes of heating (Figure 9g), the 6th row from the bottom corresponding to a temperature of 217 °F (i.e. 103 °C) underwent phase separation. At cure temperatures above 103 °C, obvious phase separation, as determined visually by changes in scattered light, were not observed. Interestingly, unlike at the other cure temperatures, the wells corresponding to a cure temperature of 95 °C (5th row from the bottom) showed a very slow increase in brightness that started at 35 minutes of cure and did not reach full brightness until the end of the experiment at 1387 minutes of curing. For samples cured at temperatures above 217 °F (i.e. 103 °C), no cloud point was observed.

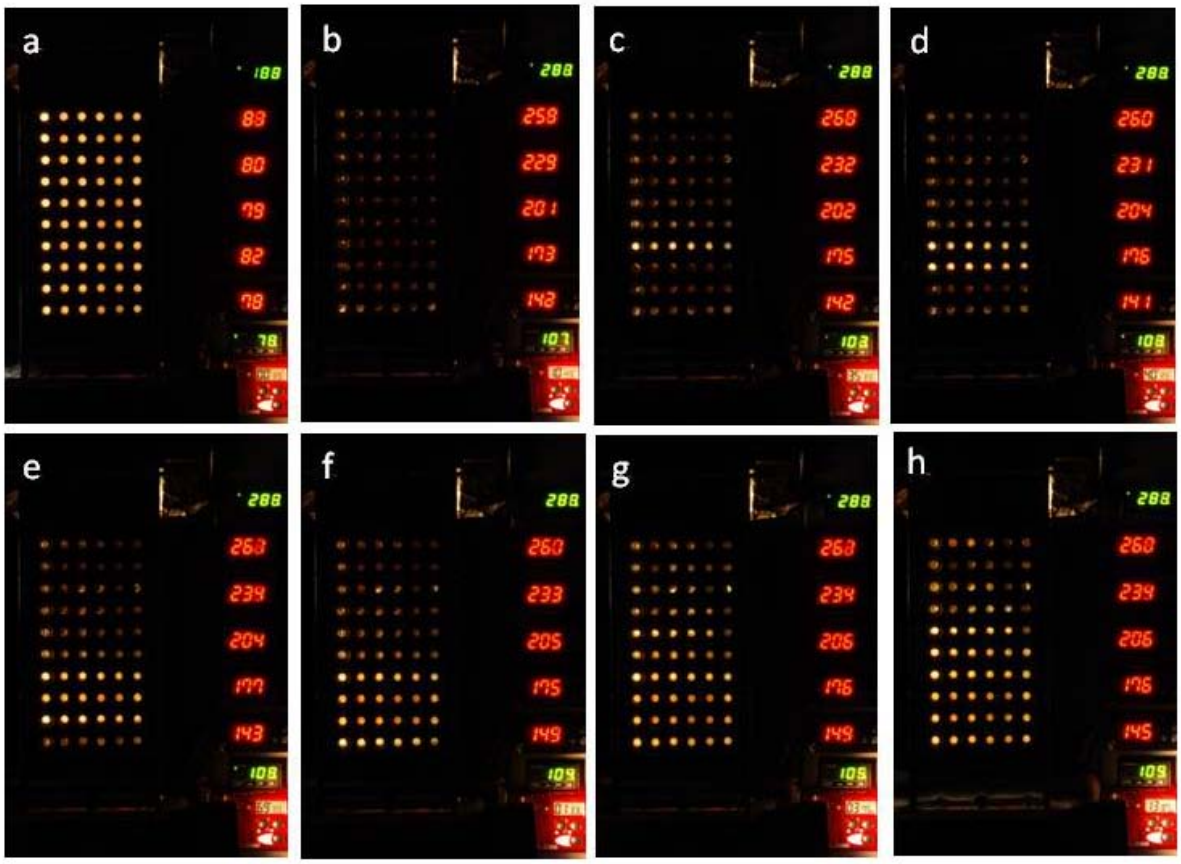

Figure 9. Representative images of the array as a function of heating time utilizing a single polymer composition across the entire array. (a) before heating (time = 0); (b) 10 minutes after the start of heating; (c) 35 minutes after the start of heating; (d) 40 minutes after the start of heating; (e) 69 minutes after the start of heating; (f) 133 minutes after the start of heating; (e) 375 minutes after the start of heating; and (h) 1387 minutes after the start of heating.

Figure 10 displays a plot that shows the time required to reach the cloud point as a function of cure temperature. This figure displays a minimum in the time require to reach the cloud point at a temperature of about 88 °C. This behavior can be attributed to the complex interactions between the rate of crosslinked network formation and the free energy of mixing. Based on the thermodynamics of mixing, increasing polymer molecular weight in a binary polymer blend exhibiting UCST phase behavior has the effect of increasing the UCST. The phase behavior observed for MCHA-60Dol showed that the cloud point without any significant curing was between room temperature and 60 °C and for essentially complete cure was between 103 °C and approximately 110 °C. Thus, the cloud point for the blend increased approximately 60-85 °C as the extent of cure increased from 0 to maximum cure. The reduction in the time required to reach the cloud point observed as a result of increasing cure temperature from 60 to 88 °C can be attributed to the relative impact temperature has on the entropy term of the Gibbs free energy and the temperature term. The increase in free energy resulting from the reduction in entropy of the

system caused by the higher degree of crosslinked network formation more than offset the reduction in free energy due simply to thermal effects. The large increase in the time required to reach the cloud point observed at a cure temperature of 103 °C can be attributed to the fact that this cure temperature is very close to the cloud point temperature observed for the essentially completely cured network and, thus, very high extents of reaction were required for phase separation to occur.

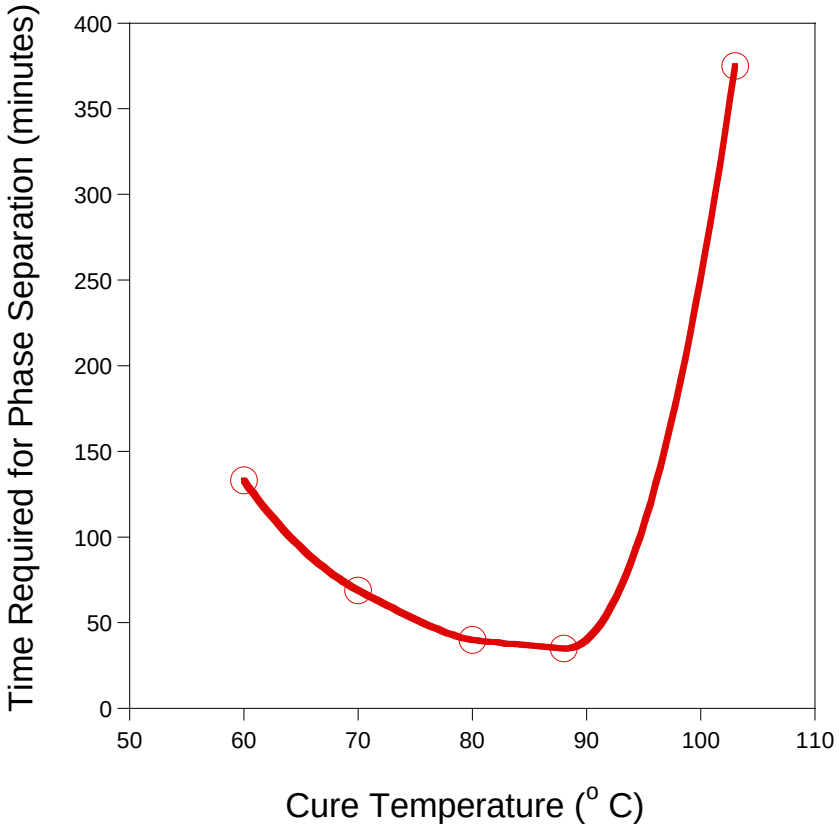

Figure 10. Time required to reach the cloud point as a function of cure temperature.

The array images obtained from the experiment provide information about relationships between cure time, temperature, and macrophase separation and allow for a quick identification of conditions that produce porosity on the micron scale. In order to obtain detailed morphological information on the porous networks, SEM was conducted. Figure 11 shows representative SEM micrographs taking from the 5th column of samples in the array shown in Figure 9. From the images shown in Figure 11, it can be easily seen that cure temperature can have a dramatic effect on sample morphology.

In general, pores formed at 80 °C and lower were spherical with average pore size appearing to decrease with increasing temperature. Between 80 °C and 103 °C, pores were irregular in shape with the degree of irregularity increasing with increasing temperature. Pore morphology over this temperature range was consistent with phase separation occurring via spinodal

decomposition. Due to the crosslinking reactions, the process of spinodal decomposition was "trapped" at different stages. The morphology of the sample cured at 103 °C was consistent with that which would be expected toward the beginning of spinodal decomposition when a cocontinuous phase morphology is produced. For samples cured at 95 and 88 °C, the morphology is consistent with later stages of spinodal decomposition in which a dispersed phase is formed, but not to the extent that spherical domains have been produced. At a cure temperature of 110 °C, morphological features can be seen in the SEM image; however, these features are very different from those at lower temperature and, thus, maybe due to the fluctuations in chemical composition that occur at the very onset of spinodal decomposition. Crosslinking may have resulted in the trapping of these local concentration gradients resulting in a more heterogeneous fracture surface compared to the fracture surfaces obtained from the true one phase materials produced at higher cure temperatures.

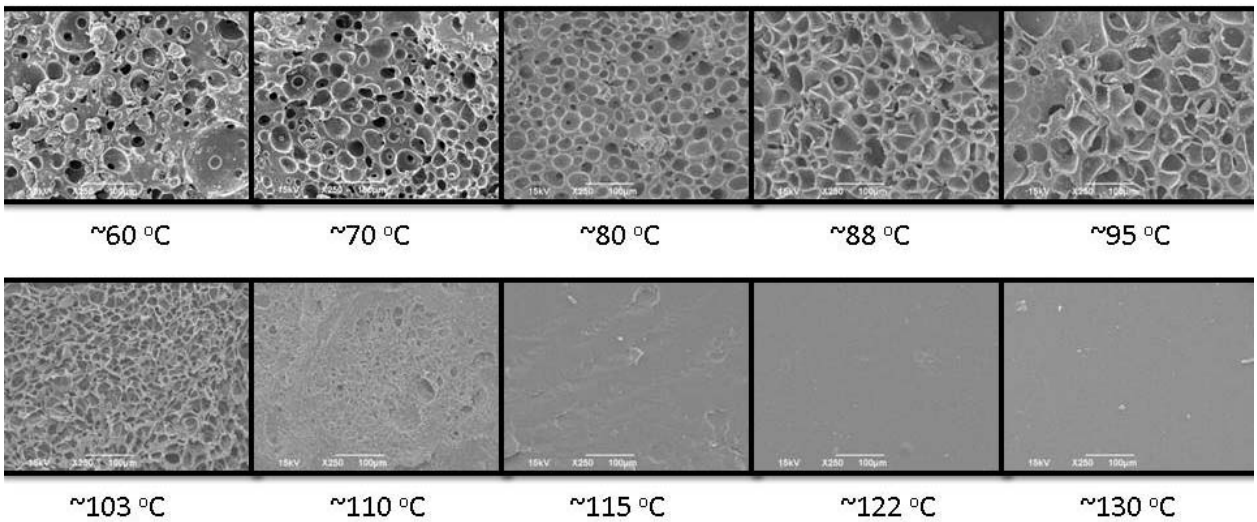

Figure 11. SEM images of poragen-extracted materials crosslinked at different temperatures. The samples were obtained from the 5th column from the left in the array shown in Figure 9.

Porous Polymer Networks Containing Conductive Particles

A series of materials were produced using both silver and nickel nanoparticles and microparticles. The crosslinked polymer matrix was produced using Ep and MCHA as the crosslinking agent. Two different poragens were used, namely, decane and decanol, and the amount of poragen was 40 volume percent. Curing was done at 40 ^{o}C. A total of 16 materials were produced, and the experimental design is shown schematically in Figure 12.

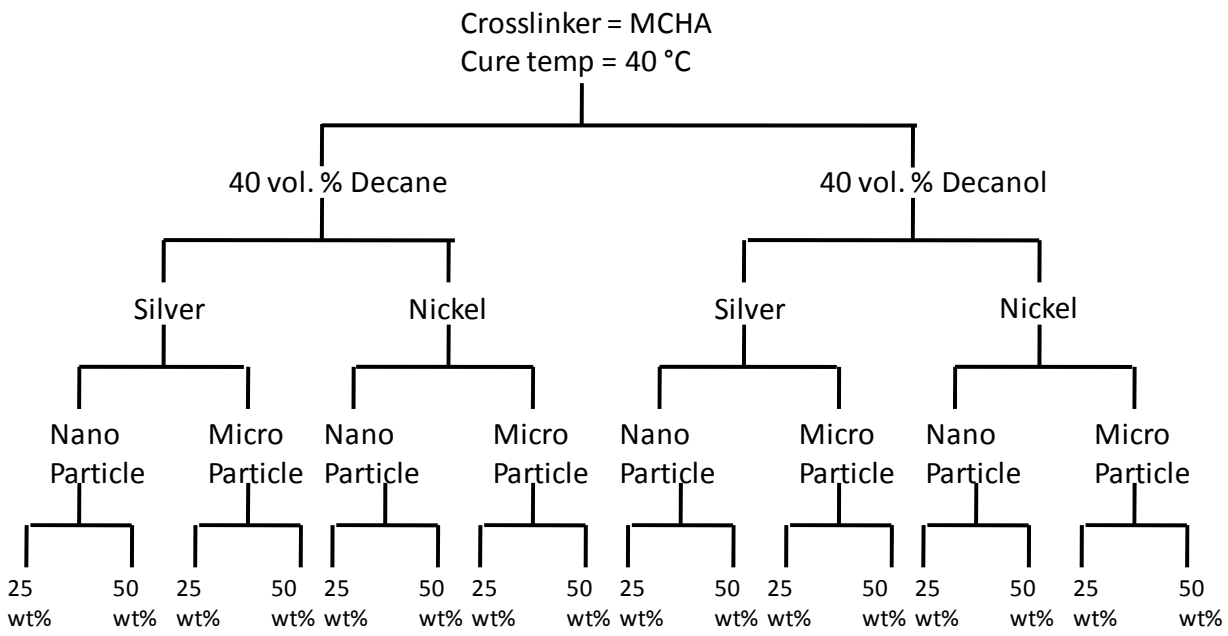

Figure 12. A schematic illustration of the experimental design used to investigate the effect of metal particles on sample morphology.

Figure 13 displays SEM micrographs of the conductive particles used for the experiment. Although the primary particles for both the silver (A) and nickel (B) nanoparticles may be in the nanometer range, the nanoparticles were highly agglomerated. This was particularly true for the silver nanoparticles. For the silver microparticles (C), particles were spherical with particle diameters around 1 micron. The nickel microparticles (D) were significantly larger than the silver microparticles and of irregular shape.

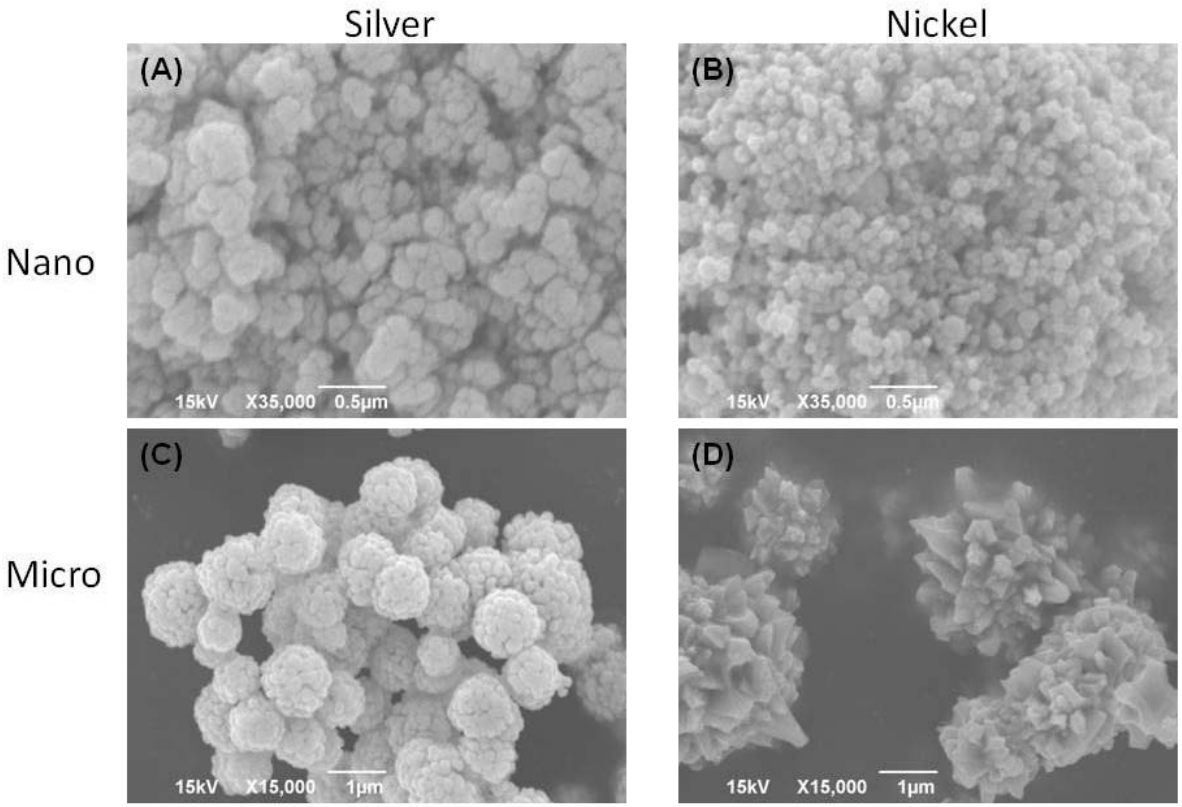

Figure 13. SEM micrographs of the metal particles used for the experiment. (A) silver nanoparticles; (B) nickel nanoparticles; (C) silver microparticles; and (D) nickel microparticles.

To characterize the level of particle dispersion that could be obtained using the method of mixing employed, composite samples containing 50 weight percent particles in the Ep/MCHA matrix were prepared. As shown in Figure 14, only the composite based on silver microparticles displayed a relatively uniform dispersion of primary particles. All other composites showed substantial agglomeration of primary particles.

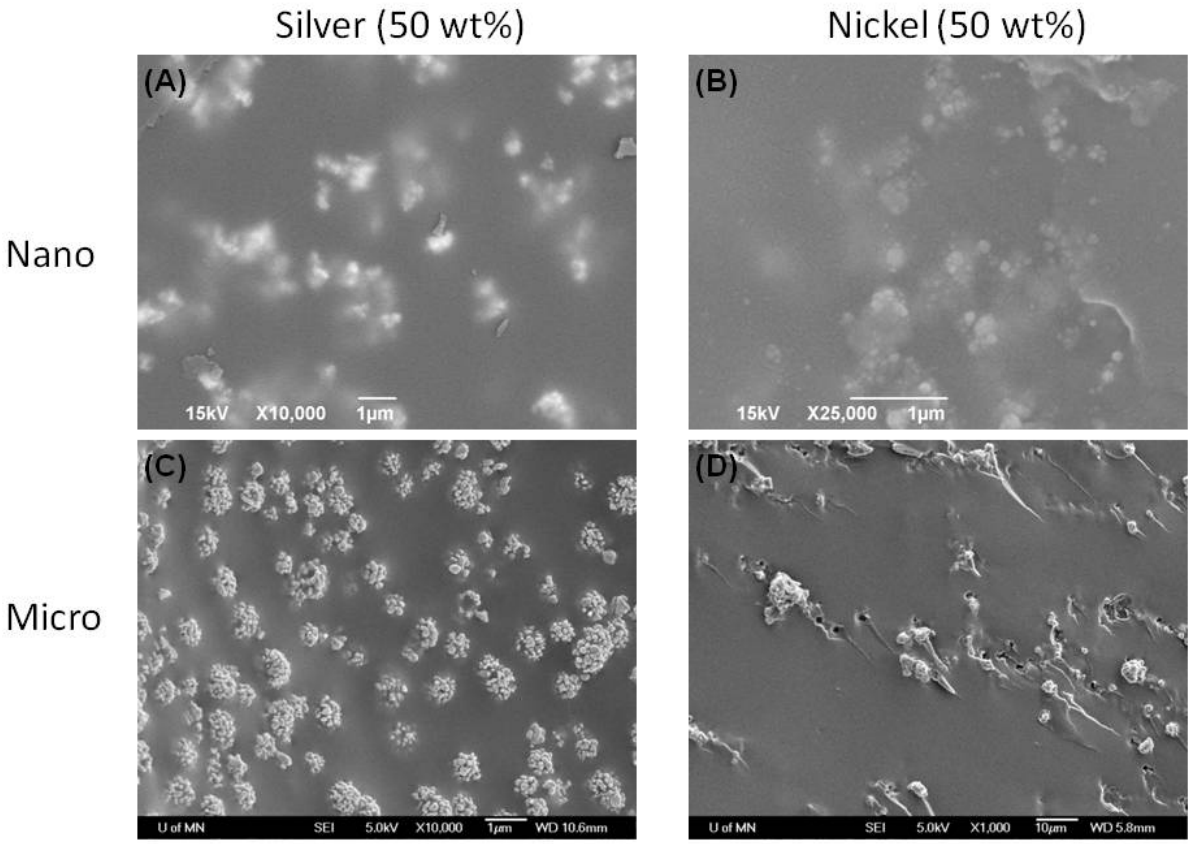

Figure 14. SEM micrographs of 50/50 wt./wt. composites of metal particles in the epoxy network. (A) silver nanoparticles; (B) nickel nanoparticles; (C) silver microparticles; and (D) nickel microparticles.

For comparison purposes, the morphology of the base porous polymer matrices (no particles) was characterized. As shown in Figure 15, the use of decane as a poragen produced a porous material consisting of isolated, spherical pores will diameters ranging from less than 1 micron to almost 10 microns. For the material based on decanol as the poragen, pore density appeared to be higher with a narrower pore size distribution and pore diameters ranging from about 2 to about 8 microns.

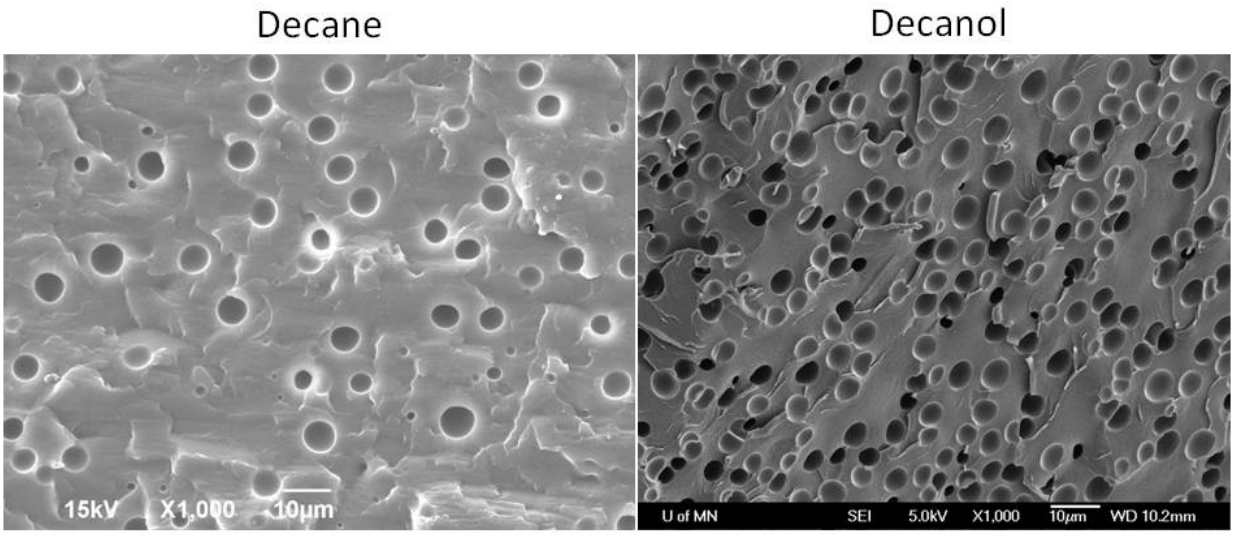

Figure 15. SEM micrographs of porous polymer networks derived from Ep/MCHA/decane (left) and Ep/MCHA/decanol (right).

Figures 16 and 17 display SEM micrographs of the porous composites based on silver nanoparticles. From the low magnification images shown in Figure 16, it can be seen that the introduction of silver nanoparticles resulted in the production of some exceptionally large pores for the composites based on decane as the poragen. For the composites based on decanol as the poragen the pore morphology did not appear to be significantly altered by the addition of the silver nanoparticles. With regard to the distribution of silver nanoparticles in the porous matrix, the images indicate that the nanoparticles were essentially exclusively contained within the polymer matrix. No evidence of nanoparticles within the pores was obtained; however, as shown in Figure 17, particles were found at the interface between pores and the polymer matrix.

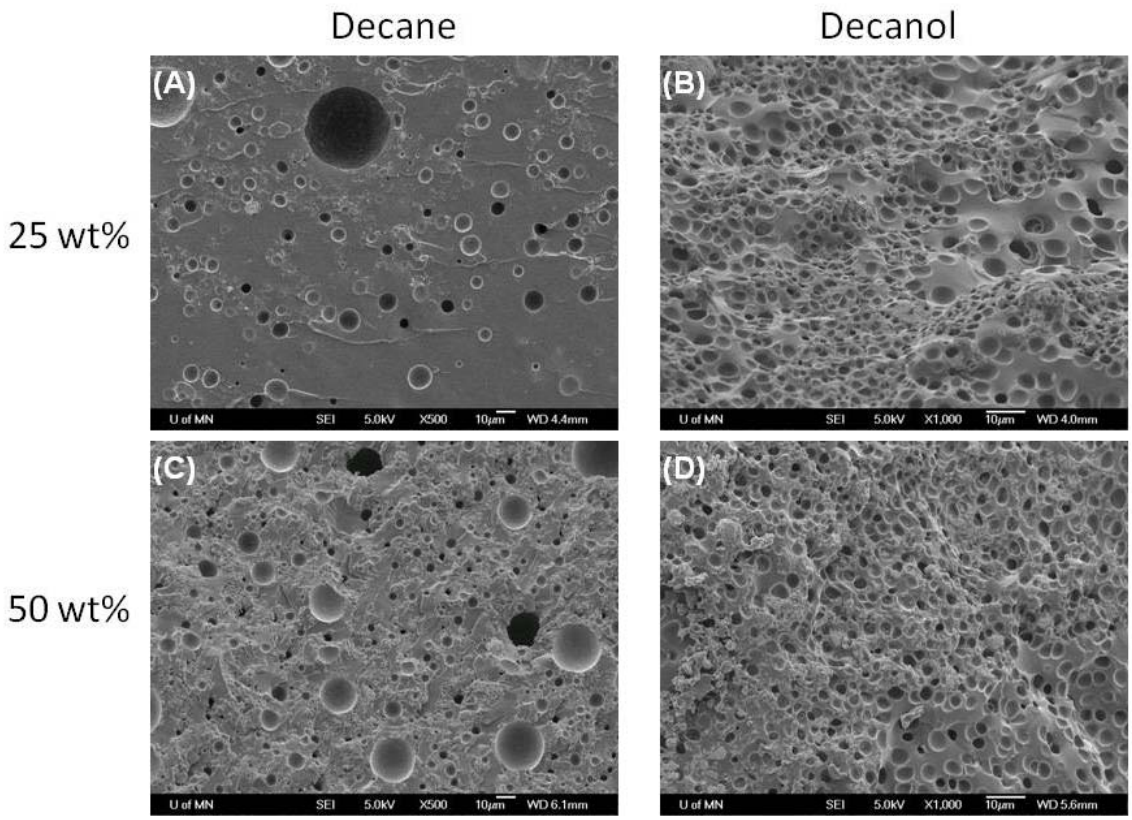

Figure 16. SEM micrographs of porous composites based on silver nanoparticles: (A) 25 wt. % Ag nanoparticles and decane as the poragen; (B) 25 wt. % Ag nanoparticles and decanol as the poragen; (C) 50 wt. % Ag nanoparticles and decane as the poragen; (D) 50 wt. % Ag nanoparticles and decanol as the poragen.

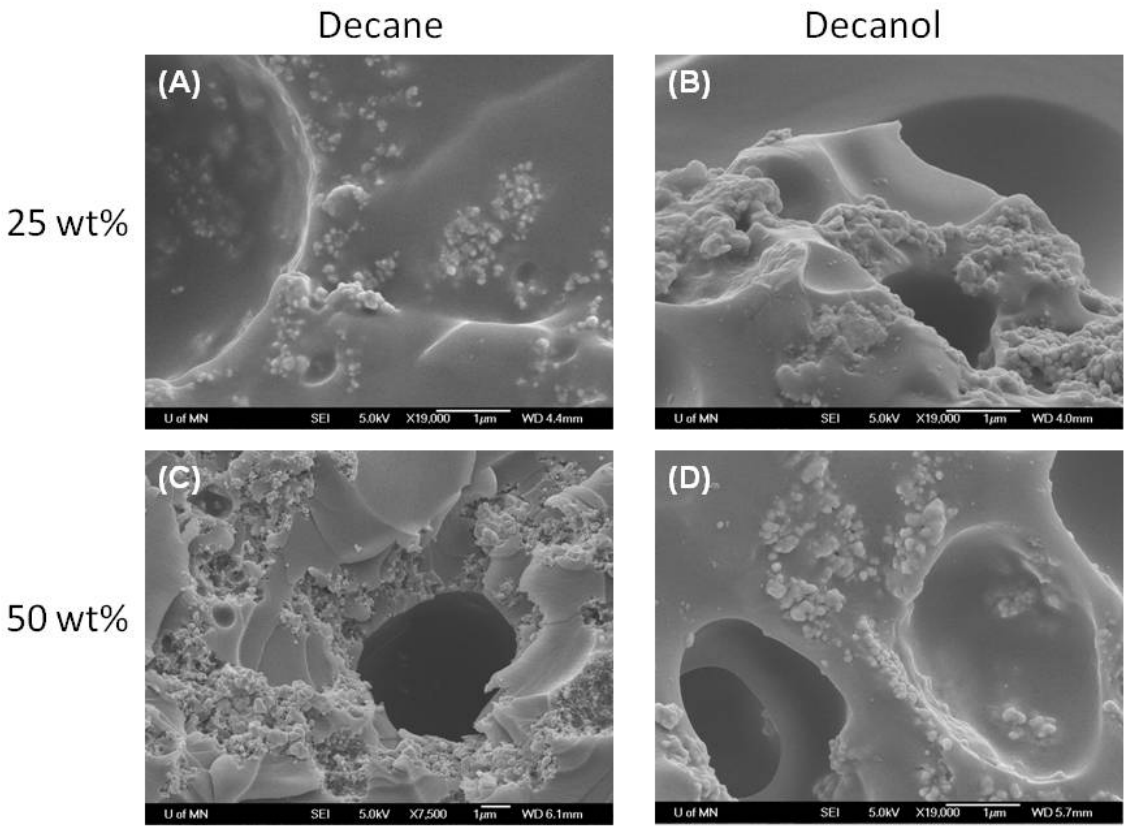

Figure 17. SEM micrographs of porous composites based on silver nanoparticles: (A) 25 wt. % Ag nanoparticles and decane as the poragen; (B) 25 wt. % Ag nanoparticles and decanol as the poragen; (C) 50 wt. % Ag nanoparticles and decane as the poragen; (D) 50 wt. % Ag nanoparticles and decanol as the poragen.

Figures 18 and 19 contain SEM images of porous composites based on silver microparticles. With regard to pore morphology, the composite derived from decanol as the poragen and containing 25 wt. % silver microparticles (Figure 18B) showed different poor morphology than the analogous materials without silver microparticles (Figure 15). With the silver microparticles, the pores were had an irregular shape. Interestingly, increasing the silver microparticle concentration to 50 wt. % produced spherical pores (Figure 18D) similar to the pores observed for the unfilled material (Figure 15). From the higher magnification images shown in Figure 19, it can be seen that a fraction of the pores contained silver particles suggesting compatibility between the silver particles and the poragens.

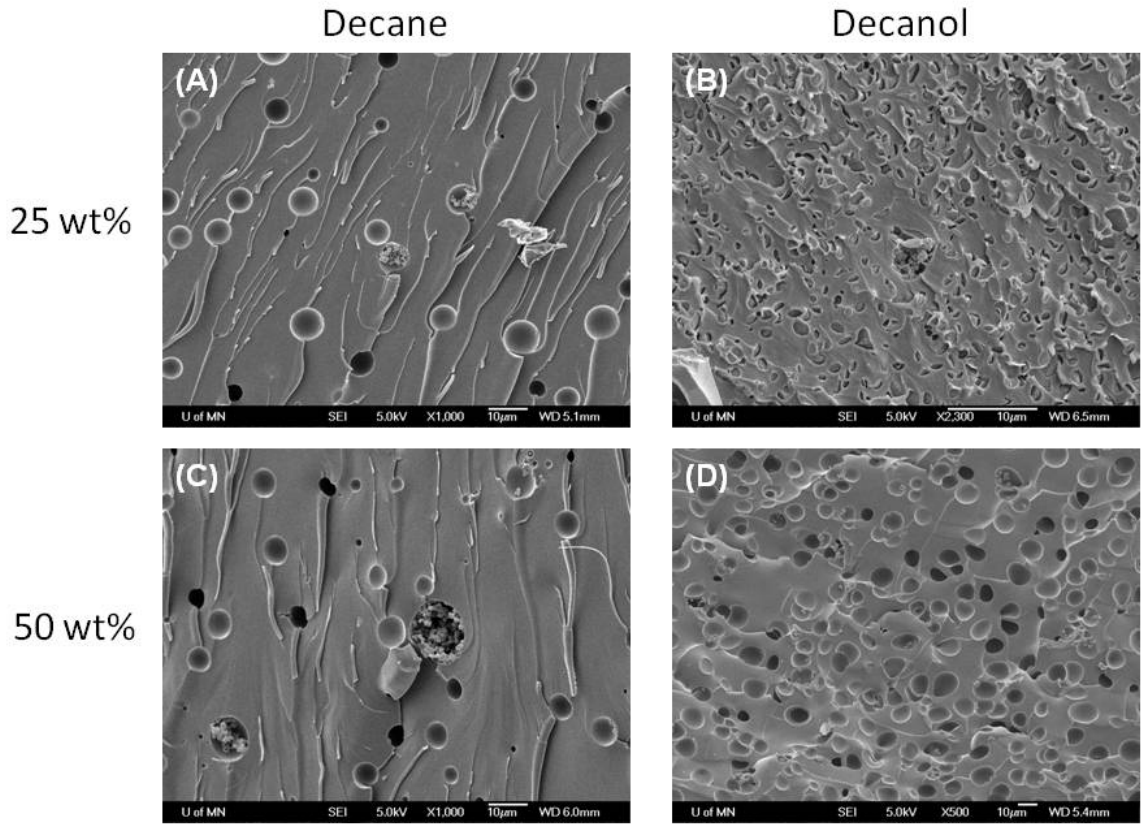

Figure 18. SEM micrographs of porous composites based on silver microparticles: (A) 25 wt. % Ag microparticles and decane as the poragen; (B) 25 wt. % Ag microparticles and decanol as the poragen; (C) 50 wt. % Ag microparticles and decane as the poragen; (D) 50 wt. % Ag microparticles and decanol as the poragen.

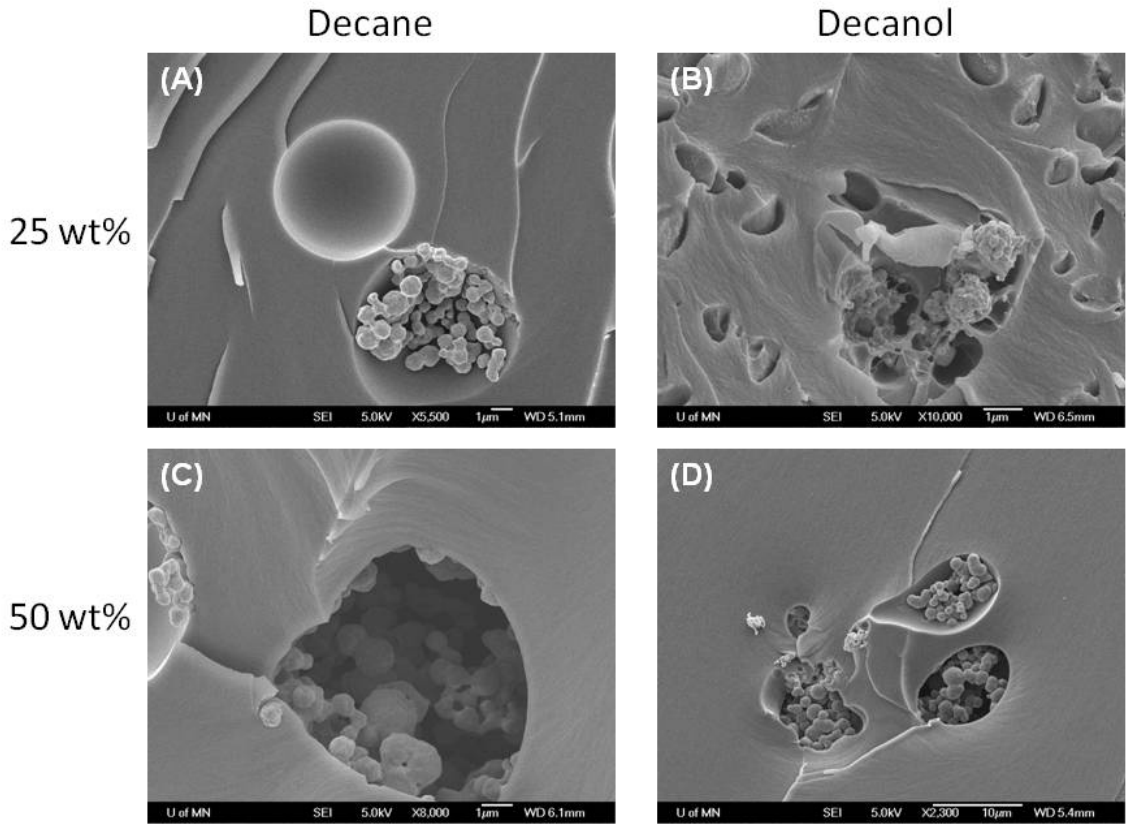

Figure 19. SEM micrographs of porous composites based on silver microparticles: (A) 25 wt. % Ag microparticles and decane as the poragen; (B) 25 wt. % Ag microparticles and decanol as the poragen; (C) 50 wt. % Ag microparticles and decane as the poragen; (D) 50 wt. % Ag microparticles and decanol as the poragen.

Figures 20 and 21 display SEM images obtained from composites based on nickel nanoparticles. Pore morphology did not appear to be significantly affected by the addition of the nanoparticles, and the nanoparticles were found be dispersed within the polymer matrix as opposed to inside the pores.

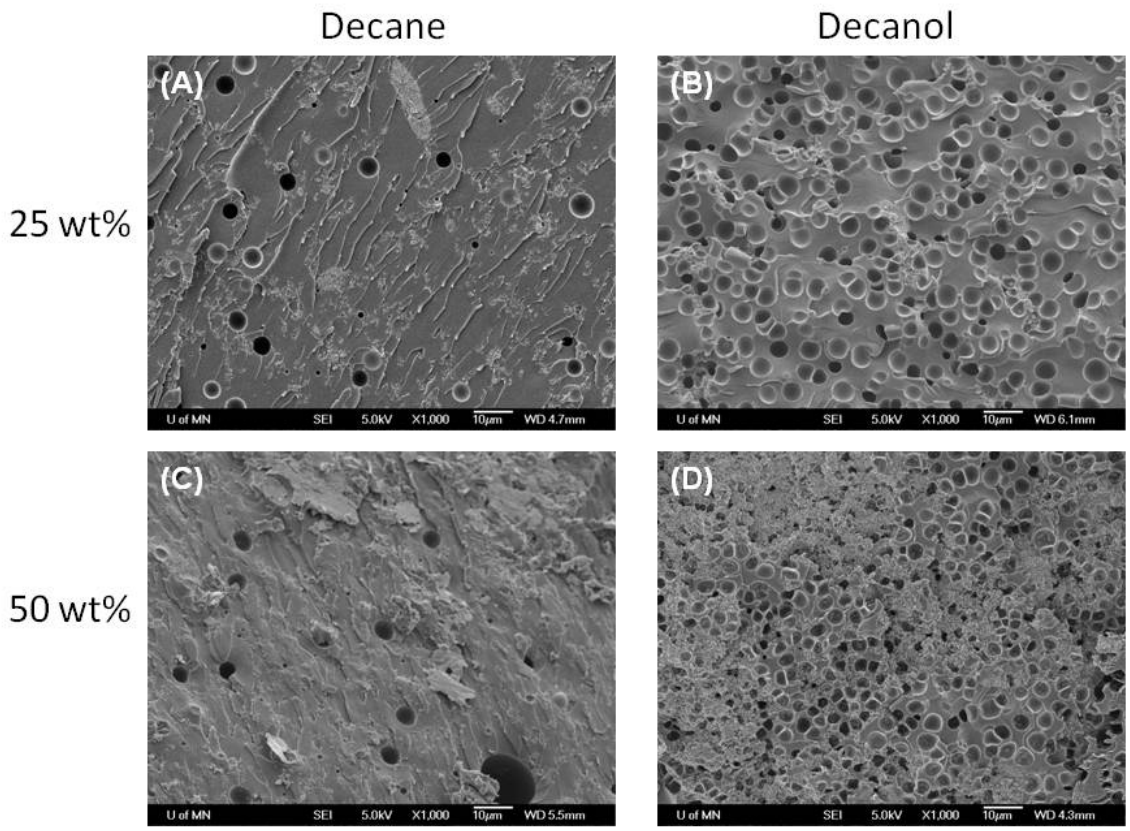

Figure 20. SEM micrographs of porous composites based on nickel nanoparticles: (A) 25 wt. % Ni nanoparticles and decane as the poragen; (B) 25 wt. % Ni nanoparticles and decanol as the poragen; (C) 50 wt. % Ni nanoparticles and decane as the poragen; (D) 50 wt. % Ni nanoparticles and decanol as the poragen.

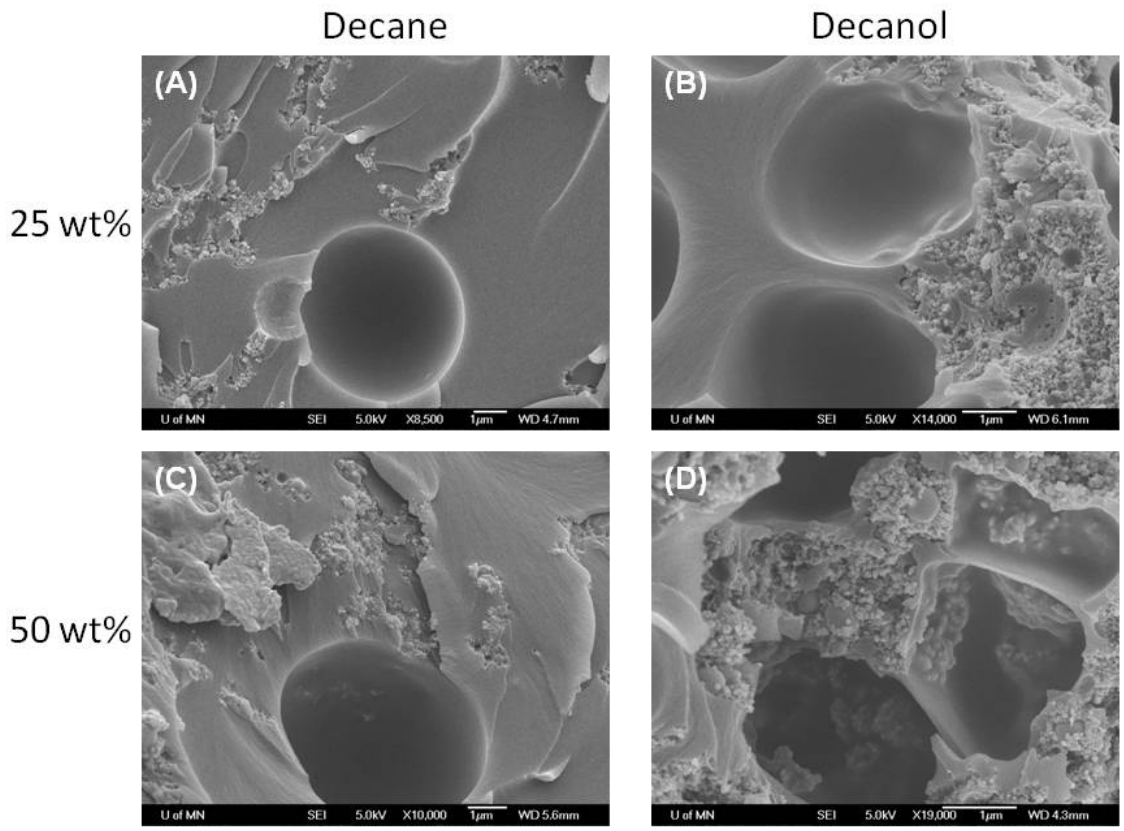

Figure 21. SEM micrographs of porous composites based on nickel nanoparticles: (A) 25 wt. % Ni nanoparticles and decane as the poragen; (B) 25 wt. % Ni nanoparticles and decanol as the poragen; (C) 50 wt. % Ni nanoparticles and decane as the poragen; (D) 50 wt. % Ni nanoparticles and decanol as the poragen.

Figures 22 and 23 display SEM images of porous composites derived from the nickel microparticles. Pore morphology was not significantly affected by the addition of the nickel microparticles. The nickel particles were found be largely dispersed within the polymer matix and highly agglomerated.

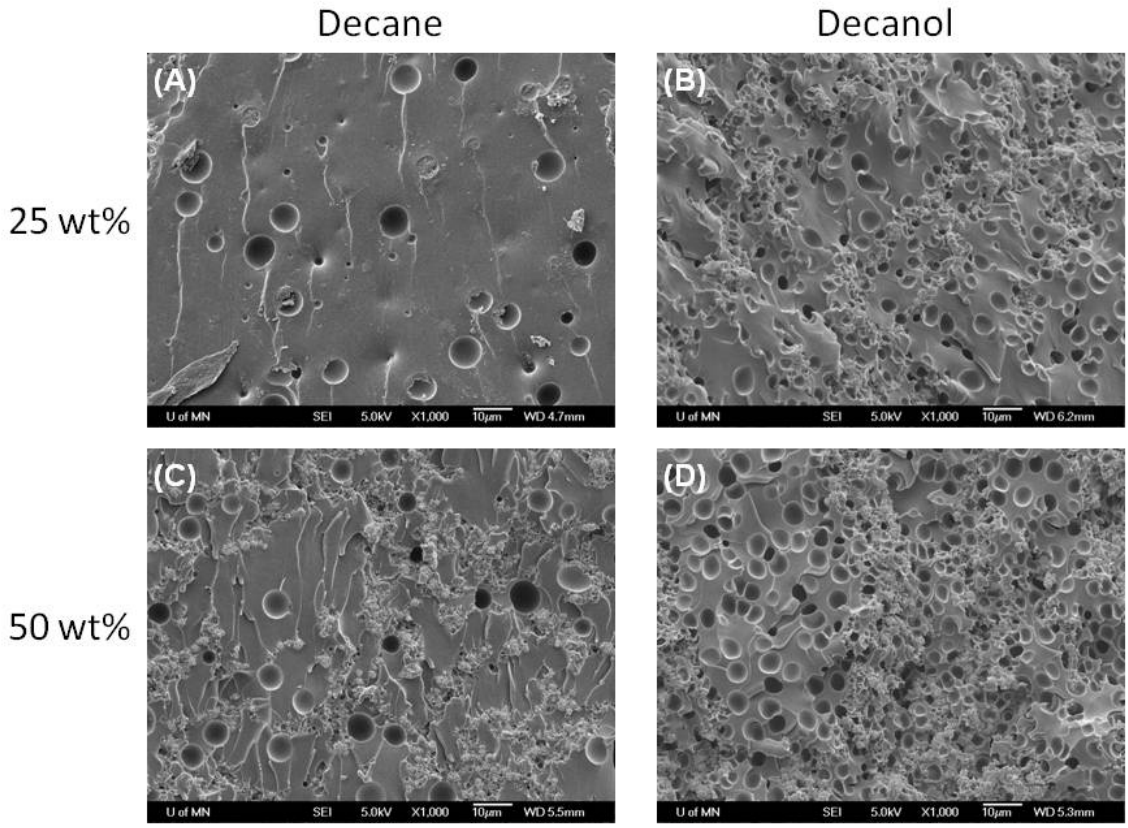

Figure 22. SEM micrographs of porous composites based on nickel microparticles: (A) 25 wt. % Ni microparticles and decane as the poragen; (B) 25 wt. % Ni microparticles and decanol as the poragen; (C) 50 wt. % Ni microparticles and decane as the poragen; (D) 50 wt. % Ni microparticles and decanol as the poragen.

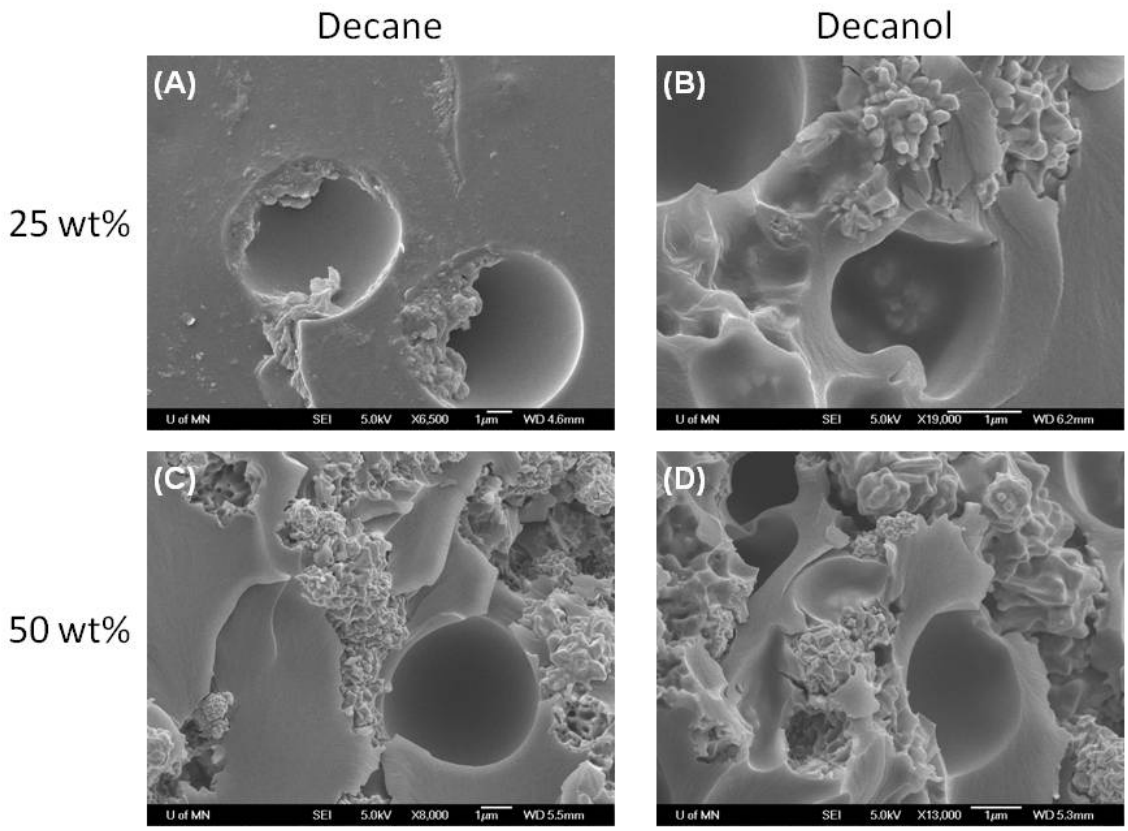

Figure 23. SEM micrographs of porous composites based on nickel microparticles: (A) 25 wt. % Ni microparticles and decane as the poragen; (B) 25 wt. % Ni microparticles and decanol as the poragen; (C) 50 wt. % Ni microparticles and decane as the poragen; (D) 50 wt. % Ni microparticles and decanol as the poragen.

4.0 Conclusions

It was shown that the gradient apparatus provides qualitative but important information that can be used to better understand the process of CIPS. Quantitative information could be obtained by improving the system with a uniform light source, CCD camera with image analysis software, and an optical table. With these modifications, the amount of scattered light from the samples could be quantified as a function of cure time and temperature. This information could be combined with sample morphological data to generate composition-process-morphology information that could potentially be used to develop models and predictive capabilities.

5.0 References

1. S. Salerno, M. Oliviero, E. Di Maio, S. Iannace, and P. Netti, “Controlled Preparation of Porous Scaffolds by Gas Foaming of Heterogeneous Blends,” AIP Conference Proceedings (2008), 1042(IVth International Conference on Times of Polymers (TOP) and Composites, 2008), 102-104.

2. P. Vandezande, L. E. M. Gevers, J. Vermant, J. A. Martens, P. A. Jacobs, I. F. J. Vankelecom, “Solidification of Emulsified Polymer Solutions via Phase Inversion (SEPPI): A Generic Way To Prepare Polymers with Controlled Porosity,” *Chem. Mater.*, 20, 3457-3465 (2008).

3. S. Eeltink, F. Svec, “Recent advances in the control of morphology and surface chemistry of porous polymer-based monolithic stationary phases and their application in CEC,” *Electrophoresis*, 28, 137-147 (2007).

4. Design of nanoporous polyarylene polymers for use as low - k dielectrics in microelectronic devices. Silvis, H. Craig; Bouck, Kevin J.; Godschalx, James P.; Niu, Q. Jason; Radler, Michael J.; Stokich, Ted M.; Lyons, John W.; Kern, Brandon J.; Marshall, Joan G.; Syverud, Karin; Leff, Mary. Corporate Research and Development, The Dow Chemical Company, Midland, MI, USA. ACS Symposium Series (2004), 874(Polymers for Microelectronics and Nanoelectronics), 187-198. Publisher: American Chemical Society, CODEN: ACSMC8 ISSN: 0097-6156. Journal written in English. CAN 141:261167 AN 2004:454825 CAPLUS

5. T. D. Li, L. M. Gan, C. H. Chew, W. K. Teo, and L. H. Gan, “Preparation of ultrafiltration membranes by direct microemulsion polymerization using polymerizable surfactants,” *Langmuir*, 12, 5863-5868 (1996).

6. Lushcheikin, G. A. Moscow State Academy of Instrumentation Technology and Informatics, ul. Stromynka 20, Moscow, Russia. Physics of the Solid State (2006), 48(6), 1023-1025. Publisher: Pleiades Publishing, Inc., CODEN: PSOSED ISSN: 1063-7834. Journal; General Review written in English. CAN 146:275247 AN 2006:585937 CAPLUS (Copyright (C) 2008 ACS on SciFinder (R))

7. V. Vamvakaki and N. A. Chaniotakis, “Immobilization of Enzymes into Nanocavities for the Improvement of Biosensor Stability,” *Biosensors & Bioelectronics*, 22(11), 2650-2655 (2007).

8. B. Adhikari and S. Majumdar, “Polymers in Sensor Applications,” *Progress in Polymer Science*, 29(7), 699-766 (2004).

9. J. Germain, J. Hradil, J. M. J. Frechet, and F. Svec, “High Surface Area Nanoporous Polymers for Reversible Hydrogen Storage,” *Chemistry of Materials*, 18(18), 4430-4435(2006).

10. J. Germain, F. Svec, and J. M. J. Frechet, “Preparation of Size-Selective Nanoporous Polymer Networks of Aromatic Rings: Potential Adsorbents for Hydrogen Storage,” *Chemistry of Materials*, 20(22), 7069-7076 (2008).

11. H. Zhao, C. Jiang, X. He, J. Ren, and C. Wan, “Preparation of Micro-Porous Membrane Electrodes and Their Application in Preparing Anodes of Rechargeable Lithium Batteries.” *Journal of Membrane Science*, 310, 1-6 (2008).

12. K. C. Khemani, Polymeric Foams: Science and Technology, American Chemical Society, Washington, DC, 1997.

13. N. R. Cameron, “High Internal Phase Emulsion Templating as a Route to Well-Defined Porous Polymers,” *Polymer*, 46, 1439-1449 (2005).

14. H. Zhang and A. I. Cooper, “Synthesis and Applications of Emulsion-Templated Porous Materials,” *Soft Matter*, 1, 107-113 (2005).

15. J. M. Torkelson and S. W. Song, “Coarsening effects on microstructure formation in isopycnic polymer solutions and membranes produced via thermally induced phase separation,” *Macromolecules*, 27, 6389-6397 (1994).

16. J. Kiefer, J. L. Hedrick, and J. G. Hilborn, “Macroporous Thermosets by Chemically-Induced Phase Separation,” *Adv. Polym. Sci.*, 147, 161-247 (1999).

17. J. S. Lee, A. Hirao, and S. Nakahama, “Polymerization of monomers containing functional silyl groups. 5. Synthesis of new porous membranes with functional groups,” *Macromolecules*, 21, 274-276 (1988).

18. G. Wulff, “Enzyme-like Catalysis by Molecularly Imprinted Polymers,” *Chem. Rev.*, 102, 1-28 (2002).

19. J. Kiefer, J. G. Hilborn, J. A. E. Manson, and Y. Leterrier, “Macroporous Epoxy Networks via Chemically Induced Phase Separation,” *Macromolecules*, 29, 4158-4160 (1996).

20. J. P. Flory, Principles of Polymer Chemistry, Cornell University Press, Ithaca, 1953.

21. M. L. Huggins, *J. Am. Chem. Soc.*, 64, 1712 (1942).

22. P. Majumdar, E. Lee, N. Patel, K. Ward, S. J. Stafslien, J. Daniels, B. J. Chisholm, P. Boudjouk , M. E. Callow, J. A. Callow, and S. E. Thompson, “Combinatorial materials research applied to the development of new surface coatings IX: An investigation of novel antifouling/fouling-release coatings containing quaternary ammonium salt groups,” *Biofouling*, 24(3), 185-200 (2008).

23. P. Majumdar, S. Stafslien, J. Daniels, and D. C. Webster, "High Throughput Combinatorial Characterization of Thermosetting Siloxane-Urethane Coatings Having Spontaneously Formed Microtopographical Surfaces," *J. Coat. Technol. Res.*, 4(2), 131-138 (2007).

24. A. Ekin and D. C. Webster, “Combinatorial and High-Throughput Screening of the Effect of Siloxane Composition on the Surface Properties of Crosslinked Siloxane-Polyurethane Coatings,” *Journal of Combinatorial Chemistry*, 9(1), 178-188 (2007).

25. http://www.fei.com/products/families/magellan-family.aspx

DISTRIBUTION

4 North Dakota State University
Attn: Bret J. Chisholm
1805 NDSU Research Park Drive
Fargo, ND 58102

1	MS0885	Justine E. Johannes	1810
1	MS0885	Carol L. Adkins	1820
1	MS0886	James H. Aubert	1822
1	MS0887	Duane B. Dimos	1800
5	MS0888	Shawn M. Dirk	1821
1	MS0899	Technical Library	9536
1	MS0123	D. Chavez, LDRD Office	1011

Sandia National Laboratories